Physical and Chemical Defects in WO_3 Thin Films and Their Impact on Photoelectrochemical Water Splitting

Y. Zhao [a], S. Balasubramanyam [b], R. Sinha [a], R. Lavrijsen [c], M.A. Verheijen [b], A. A. Bol [b], A. Bieberle-Hütter [a]

[a] *Electrochemical Materials and Interfaces (EMI), Dutch Institute for Fundamental Energy Research (DIFFER), 5600 HH Eindhoven, The Netherlands*

[b] *Plasma and Materials Processing (PMP), Department of Applied Physics, Eindhoven University of Technology (TU/e), 5600 MB Eindhoven, The Netherlands*

[c] *Physics of Nanostructures and center for NanoMaterials (cNM), Department of Applied Physics, Eindhoven University of Technology (TU/e), 5600 MB Eindhoven, The Netherlands*

Corresponding author: A. Bieberle-Hütter, e-mail address: A.Bieberle@differ.nl

Abstract

We evaluate the impact of defects in WO_3 thin films on the photoelectrochemical (PEC) properties during water splitting. We study physical defects, such as micro holes or cracks, by two different deposition techniques: sputtering and atomic layer deposition (ALD). Chemical defects, such as oxygen vacancies, are tailored by different annealing atmospheres, i.e. air, N_2, and O_2. The results show that the physical defects inside the film increase the resistance for the charge transfer and also result in a higher recombination rate which inhibits the photocurrent generation. Chemical defects yield in an increased adsorption of OH groups on the film surface and enhance the PEC efficiency. Excess amount of chemical defects can also inhibit the electron transfer, thus decreasing the photocurrent generation. In this study, the highest performance was obtained for WO_3 films deposited by ALD and annealed in air, which have the least physical defects and an appropriate amount of oxygen vacancies.

Keywords: WO_3, atomic layer deposition (ALD), sputtering, defects, electron transport, photoelectrochemical water splitting

1. Introduction

Converting sunlight into chemical fuels is a promising pathway for the utilization of renewable energy, which could potentially ease the dependence on fossil fuels and contribute to resolving global warming[1–3]. Hydrogen production from photoelectrochemical (PEC) water splitting using semiconductor photoelectrodes has been widely studied since the first discovery in 1972[4].

During the past decades, great effort has been devoted towards exploiting efficient and robust photoelectrode materials[5–9]. As a photoanode material, tungsten oxide (WO_3) has been strongly investigated due to its high electron mobility (~12 $cm^2V^{-1}s^{-1}$ at RT), suitable band-gap (2.6-2.9 eV), and good chemical stability[10–13].

Despite these promising features, the conversion efficiency of the reported WO_3 photoanodes is still far below the theoretical maximum conversion efficiency of 6.3%[14–18]. This is attributed to its low light harvesting efficiency and high electron-hole recombination rate. Several studies have focused on overcoming these issues, such as selective doping of metal and non-metal semiconductors[19,20], adding of co-catalysts, like CoO_x or Co-Pi, to improve the water oxidation kinetics[21,22], forming a heterojunction via introduction of another semiconductor layer, like $BiVO_4$, Bi_2S_3, Cu_2O, to enhance the electron transport properties[23–25], or using nano/micro-structured substrates[26,27]. Various thin film deposition techniques have been used to achieve improved film structures, including hydrothermal method[28], sputtering[29], pulsed laser deposition (PLD)[30], and atomic layer deposition (ALD)[14].

Another important aspect that has not been paid enough attention yet is that the quality of the thin film can significantly affect the PEC properties. During PEC water splitting, the photo-excited holes are transferred from the bulk to the surface of the WO_3 film for water oxidation, while the electrons are transferred to the external circuit through the functional thin film. Thus, physical defects, such as micro holes or cracks in the film can impact the photocatalytic activity and charge transfer efficiency[11,14]. It is known in PEC water splitting that open porosity can increase the conversion efficiency by increasing the specific surface area[11,31,32]. However, the physical defects inside the film and the interface between the functional layer and the electron collecting layer can also impede electron transport which is often not considered. Chemical defects, such as oxygen vacancies, play a sensitive role in photocatalysis as well[33–35]. Oxygen vacancies in WO_3 films can act for example as electron donor to enhance the PEC efficiency[12,36]. In recent density functional theory (DFT) studies on the electrochemical activity of WO_3 and Fe_2O_3, oxygen vacancies were found to strongly impact the overpotential[37,38]. A reduction of the overpotential of 0.2 V was found for Fe_2O_3 (110) in[38] depending on the density of oxygen vacancies. The overpotential is a measure for the electrochemical activity and has therefore direct impact on the performance. Hence, the performance can be tailored by the chemical defects. Systematic, experimental studies on the impact of oxygen vacancies related to the electrode processing have not been done so far. It is therefore important to relate the physical and chemical defects of the WO_3 film

to the PEC properties and from this to conclude about how to design and fabricate high performing electrodes for PEC water splitting.

To this aim, we systematically evaluate the impact of defects in WO_3 thin films on the PEC properties during water splitting. We study the physical defects by comparing the properties of WO_3 thin films deposited by sputtering and ALD, respectively. The chemical defects are evaluated by different annealing atmospheres (air, N_2 and O_2). By this, systematic insight into the relation between film quality and PEC performance of thin film photoelectrodes is gained which will guide towards design rules for high performing photoelectrodes

2. Experimental section

2.1. WO_3 films deposition

WO_3 thin films were deposited by reactive radio frequency (RF) sputtering and by plasma-enhanced ALD on commercial fluorine-doped tinoxide (FTO) (about 400 nm) coated 1 mm thick glass substrates (FTO15, Pilkington). Before the deposition, the substrates were cleaned following the procedure described in Malviya et al[39]. Sputtered WO_3 films were deposited by a RF sputtering tool from Kurt J. Lesker using a 2 in. metallic tungsten target with a target-substrate distance of 95 mm. The main deposition parameters are listed in Table 1.

A FlexAL ALD reactor from Oxford Instruments, equipped with an inductively coupled plasma (ICP) source, was used to deposit WO_3. The metalorganic precursor $(^tBuN)_2(Me_2N)_2W$ (99% purity, Sigma Aldrich) was used as the tungsten source and O_2 plasma was used as the co-reactant. The main parameters of the ALD process are listed in Table 2. The plasma enhanced ALD process is described in detail in[40].

Table 1

Sputtering process parameters for WO_3 deposition.

Parameter	Value
Target power	100 W
Base pressure	$<10^{-8}$ mbar
Deposition pressure	10^{-2} mbar
Substrate temperature	Room temperature

O_2 flow rate	10 sccm
Ar flow rate	40 sccm

Table 2

ALD process parameters for WO_3 deposition.

Parameter	Value
Base pressure	$<10^{-6}$ mbar
Table temperature	300℃
O_2 plasma power	250 W
Precursor dosing	3 s
Coreactant O_2 plasma exposure	3 s

2.2. Annealing

All WO_3 films were annealed at 450℃ for 1 h with a ramping rate of 5℃/min using a tubular furnace with quartz tube (Carbolite Gero). Different annealing atmospheres were used by tuning the gas flow rate: pure N_2 (15 sccm), and pure O_2 (15 sccm) and air (12 sccm N_2 mixed with 3 sccm O_2). The gas flow was started 30 min prior to the annealing to guarantee a stable gas atmosphere.

2.3. Thin film characterization

The morphologies of the films were investigated by a field emission scanning electron microscope (SEM) (Zeiss Sigma, Germany) with an in-lens detector and 5 kV accelerating voltage and a probe corrected JEOL ARM200F transmission electron microscope (TEM) operated at 200 kV in high angle annular dark field (HAADF) scanning TEM (STEM) mode. Cross-sectional TEM sample preparation was performed using a focused ion beam (FIB) (FEI, the Netherlands) using a standard lift-out procedure. The crystalline phase of the thin films was characterized by a Bruker D8 Eco X-ray diffractometer (XRD) with a Cu Kα (λ = 1.5406 Å) source and a Lynx-eye detector in a grazing incidence configuration at an incident angle of 3° and in the 2θ range from 20° to 60°. The elemental compositions and the valence states of elements were analysed using a Thermo Scientific Kα X-ray photoelectron spectroscopy (XPS) setup with an Al Kα source (hν = 1486.6 eV). The binding energy was calibrated according to the

signal of adventitious carbon (binding energy = 284.8 eV). The light transmittance and absorbance of the films were investigated using a Perkin Elmer 1050 UV/Vis/NIR Spectrophotometer in the wavelength range of 250 nm to 800 nm with a step of 5 nm.

2.4. Photo-electrochemical characterization

The PEC performance was measured using a three-electrode PEC cell with a quartz window at room temperature. Illumination was provided by an AM 1.5 class A solar simulator (LCS 100, Oriel Instruments) using a 100 W Xe lamp with a calibrated illumination intensity of 100 mW cm^{-2} at the sample position. The light sources was calibrated with a calibrated reference cell and meter (Newport, model 91150V). The WO_3 thin films on FTO glass substrates (working electrodes) were encapsulated in epoxy (Loctite EA 9492) resulting in an exposed active area of about 0.3 cm^2. Calibrated digital images and ImageJ were used to determine the exact geometrical area of the exposed electrode surface. A coiled Pt wire (0.8 mm in thickness) and an Ag/AgCl/Sat. KCl electrode (XR 300, Radiometer Analytical) were used as the counter and reference electrode, respectively. An aqueous solution of 0.5 M H_2SO_4 (pH ~0.3) was used as electrolyte. The potential of the electrode was controlled with a BioLogic SP-150 potentiostat. All potentials reported in this study are given versus reversible hydrogen electrode (RHE) through the relation[41]

$$\Phi_{RHE} = \Phi_{Ag/AgCl} + \Phi^{o}_{Ag/AgCl\ vs\ RHE} + 0.059 \times pH \qquad (1)$$

with $\Phi^{o}_{Ag/AgCl}$ is 0.197 V versus RHE at 25°C. Linear sweep voltammetry (LSV) measurements were performed at potentials between 0.4 V and 1.6 V versus RHE at a scan rate of 10 mV s^{-1} under chopped incident light with an externally controlled shutter with a rate of 0.5 s^{-1}. Electrochemical impedance spectroscopy (EIS) was carried out in the frequency range between 0.01 Hz and 10 kHz with an AC bias signal of 10 mV at a single constant potential (1.0 V vs. RHE) under simulated sun light irradiation. Intensity modulated photocurrent spectroscopy (IMPS) measurements were conducted using a Modulab Xm PhotoEchem potentiostat (Solartron Analytical) in the same cell and electrolyte as previously mentioned. Modulated illumination was provided by a high intensity light emitting diode (λ_{LED} = 405 nm) controlled by a LED driver (Thorlabs) that allowed the superimposition of sinusoidal modulation (~ 10%) on a DC illumination. The density of DC illumination was adjusted to 40 mW cm^{-2}. The bias potential was maintained at 1.23 V vs. RHE during the IMPS measurements.

3. Results and Discussion

3.1. Structural and optical properties

The GIXRD spectra of the ALD and sputtered films after annealing in air at 450°C for 1 h are shown in Figure 1. The diffraction peaks of the films agree well with monoclinic WO_3 corresponding to JCPDS No. 83-0950, indicating that monoclinic WO_3 was obtained from both ALD and sputtered WO_3 film after annealing. The ALD WO_3 film, however, has a preferred orientation in the [002] direction, while the sputtered WO_3 film is randomly oriented. The average vertical diameter d of the grains was calculated from the XRD line width using the Scherrer equation, $d = 0.9\lambda/(\beta\cos\theta)$, where λ is the X-ray wavelength, β is the full width at half-maximum (FWHM) of the diffraction peak, and θ is the diffraction angle. Values of d were calculated from the FWHM of the [002] peaks for sputtered and ALD WO_3 resulting in similar average vertical diameters of 28.2 nm and 30.4 nm, respectively.

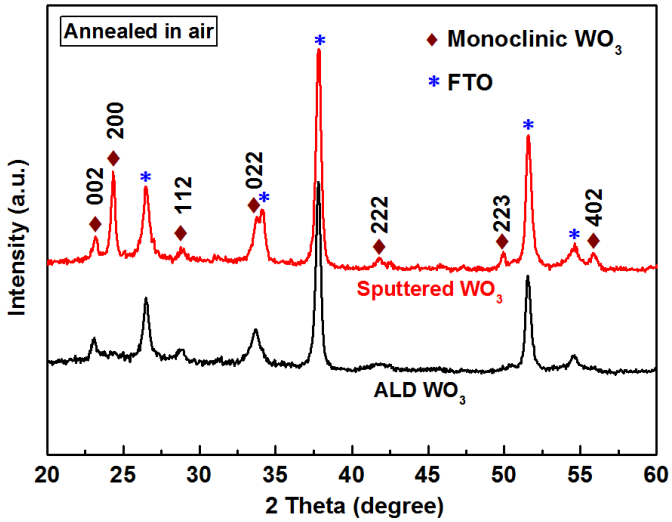

Figure 1. GIXRD spectra of ALD (black) and sputtered (red) WO_3 thin films after annealing in air. The brown diamonds and the blue dots are monoclinic WO_3 (JCPDS No. 83-0950) and FTO (JCPDS No. 83-0950), respectively.

The optical properties of the WO_3 thin films were investigated by UV-vis spectrophotometry. Figure 2a shows the transmittance spectra of the ALD and the sputtered WO_3 thin films. It is found that the optical transmittance of the ALD film is slightly lower than that of the sputtered film. This can be attributed to the more compactly arranged WO_3 grains in the ALD film, since the film thicknesses were similar. The optical indirect band gap of the WO_3 thin films was obtained by Tauc analysis[42] from the transmittance spectra according to the following equation:

$$(\alpha h\nu)^{1/2} = C(h\nu - Eg) \quad (2)$$

where α is the optical absorption coefficient (-[1/d]ln[T/100]), d is the film thickness, T is the optical transmittance, $h\nu$ is the incident photon energy, C is a

constant, and E_g is the optical indirect band gap energy. The optical indirect band gap of ALD and sputtered WO_3 thin films were obtained by extrapolation to the abscissa of the plot of $(\alpha hv)^{½}$ against hv. As shown in Figure 2b, the optical indirect band gap of the ALD and the sputtered WO_3 film were both close to 3.0 eV. The band gap values correspond to the reported band gap range for bulk material in the literature (2.5 – 3.1 eV)[40,42–44].

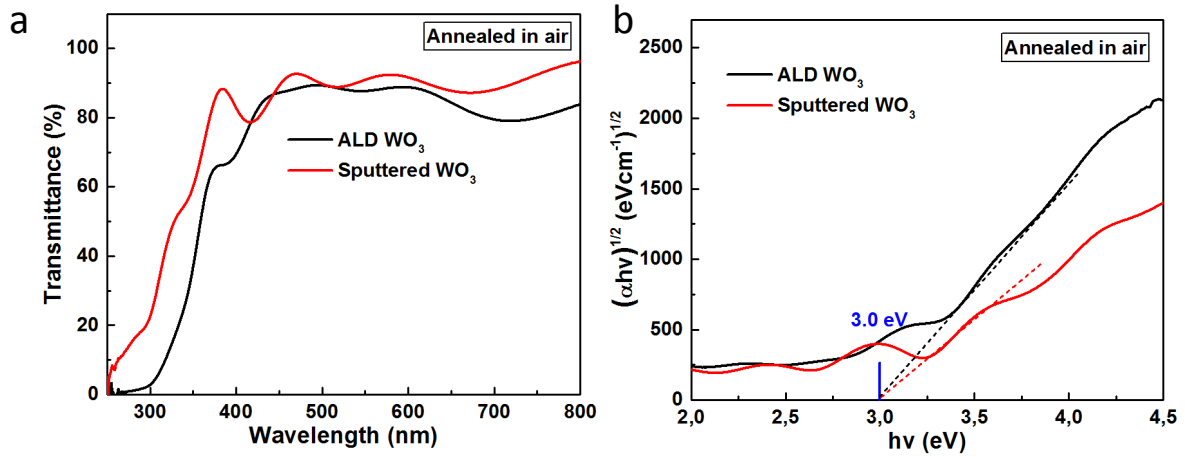

Figure 2. (a) Transmittance spectra of ALD (black) and sputtered (red) WO_3 thin films annealed in air. (b) Tauc plots of the same films.

3.2. Physical defects

Physical defects, like micro-cracks, micro-holes, or disrupted structure, affect the quality of the functional thin films, especially on their application in photocatalysis[45–47]. In the following, we evaluate the physical defects by comparing the properties of ALD and sputtered WO_3 thin films.

The microstructures of the ALD and sputtered WO_3 thin films after anealing in air is shown in Figure 3. The surface morphologies of ALD and sputtered WO_3 films are shown in Figure 3a and Figure 3b, respectively. The WO_3 grains of the ALD thin film have a rounded shape with a size of around 100 nm in diameter. The grains are more homogeneous and compactly arranged than the grains in sputtered WO_3 films. The shapes of the sputtered grains are sharp which is similar to the FTO grains (Figure S1). Many micro-holes are visible around the grains. No significant difference in the surface roughness between ALD and sputtered films was found, as proven by Atomic Force Microscope (AFM) images in Figure S2. The surface roughnesses were R_a = 3.4 nm and R_a = 4.9 nm for the ALD and the sputtered films, respectively. Figure 3c and 3d show the STEM images of the cross-sections (lower magnification images in Figure S3). The thicknesses are around 50 nm for both ALD and sputtering films. Both ALD and sputtered films show continuous layer coated on the FTO grains. However, for sputtered WO_3, nano-size holes are distributed inside the film and the interface

between WO_3 and FTO layer, as shown as the dark spots in Figure 3d. While for ALD WO_3 film, no obvious micro holes or the other physical defects were observed. Schematic sketches are shown in Figure 3e and Figure 3f to illustrate the different structures formed by ALD and sputtering, respectively.

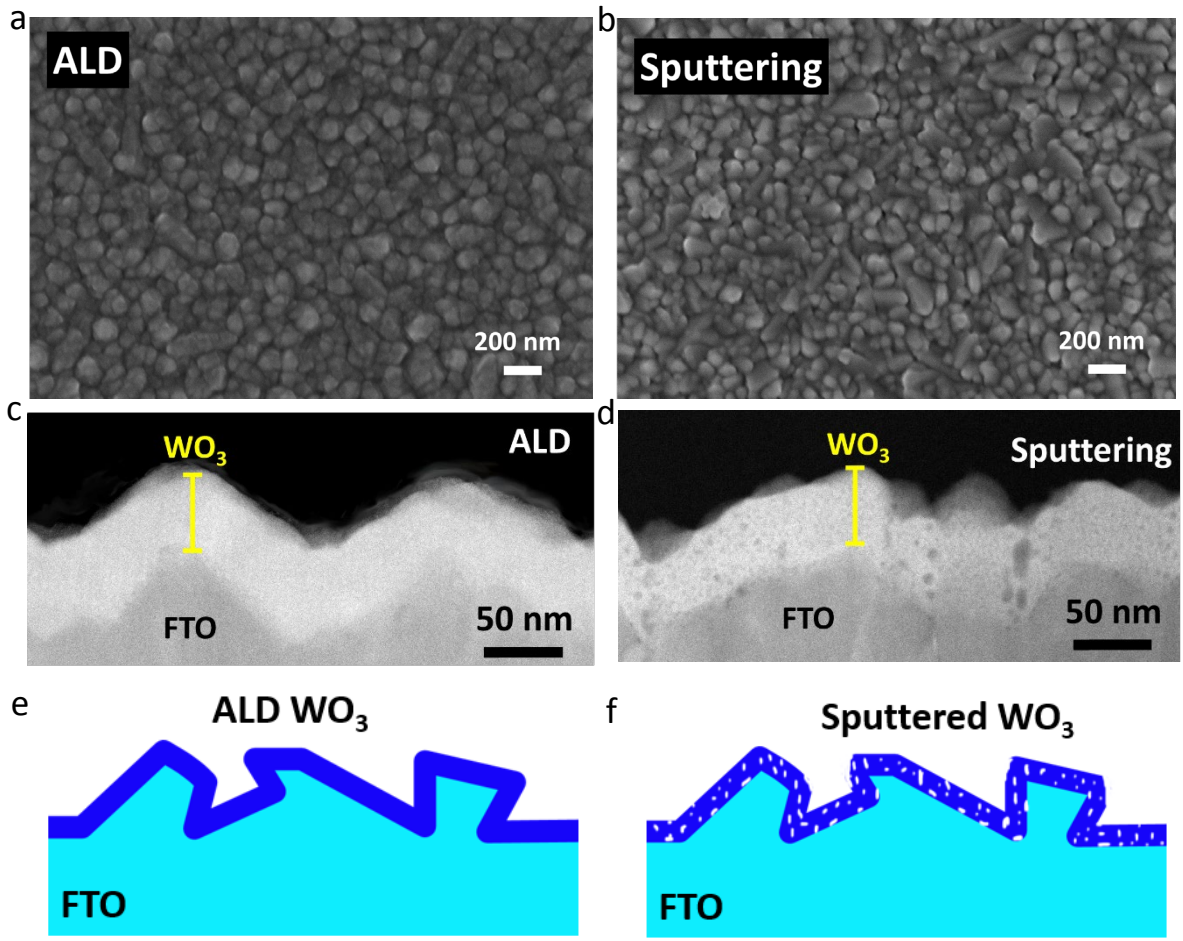

Figure 3. Top view SEM images of WO_3 thin film after annealing in air deposited by (a) ALD and by (b) sputtering; cross-section HAADF-STEM images of (c) ALD and (d) sputtered WO_3 thin films after annealing in air; schematic sketches of the cross sections of (e) ALD and (f) sputtered WO_3 thin films.

The PEC activity of the ALD and sputtered WO_3 thin films were compared by measuring the photocurrent as a function of the applied potential (0.4 - 1.6 V vs. RHE) in 0.5 M H_2SO_4 under chopped AM 1.5 illumination. A photocurrent density of 0.10 mA/cm^2 at 1.23 V vs. RHE was obtained from the ALD WO_3 thin film (Figure 4a). This is significantly higher than the photocurrent density of 0.06 mA/cm^2 at 1.23 V vs. RHE for the sputtered film. As shown in Figure 4a, the dark current obtained from the sputtered WO_3 film begins to rise at 1.35 V vs. RHE, while for the ALD film the dark current remains negligible in the entire range of applied potentials. The reason can be due to the micro holes inside the film, which resulted in that the FTO was exposed to the electrolyte during the PEC measurement.

In the literature, the highest photocurrent reported was about 1.5 mA/cm^2 at 1.23 V vs. RHE for 180 nm thick films in 1M KCL electrolyte (with HCl added to adjust the pH from 2 to 7) deposited by ALD[14]. This higher performance is attributed to the considerably thicker films and the different electrolyte. WO_3 has a large hole diffusion length (ca. 150 nm)[48]. Therefore, within a certain range, thicker films can harvest more light without causing a significantly increase in charge recombination rate[29]. For sputtered WO_3 films reported from the literature, the photocurrent densities of flat WO_3 in the literature scattered between 0.03 mA/cm^2 and 0.1 mA/cm^2 at 1.23 V vs. RHE, which were measured by the same method with film thicknesses between 100 nm and 500 nm[29,49]. Hence, our sputtered WO_3 thin films with a thickness of only 50 nm are higher quality than those mentioned in current literature.

The higher photocurrents obtained from ALD WO_3 films in this study can be attributed to three factors: The first and the main factor is that due to its self-limiting nature, the ALD films have a more perfect interface with the FTO and less physical defects inside the film (refer to Figure 3). Physical defects can act as obstacles for the photo-generated charge carrier transfer. This is confirmed by the impedance measurements at a single constant potential (1.0 V vs. RHE) under continuous light illumination (under dark condition in Figure S4). As shown in Figure 4b, the plots represent the experimental data and the solid lines represent the fitting results. The data was fitted with an equivalent circuit consisting of a resistance (R_{series}) and two RC elements ($R_{SC}C_{Bulk}$ and $R_{CT}C_H$) in series (inset in Figure 4b). The EIS spectra at the high frequency ($R_{SC}C_{Bulk}$) is assigned to the electronic processes occurring in the WO_3 bulk[49]. The low frequency part of the spectrum ($R_{CT}C_H$) is assigned to the phenomena occurring at the WO_3/electrolyte interface[50]. The fitting values of the overall resistance ($R_{series} + R_{SC} + R_{CT}$) of the ALD WO_3 photoelectrode is 18 kΩ which is lower than that of sputtered WO_3 being 28 kΩ.

The second factor is related to the preferred (002) orientation of the ALD film (Figure 1). It is reported that the (002) facets of monoclinic WO_3 remarkably enhance the electron mobility by reducing the recombination of electron-hole pairs[51–53], which was attributed to its lower free energy changing in the electron transfer[15,54]. Third, the slightly higher light harvesting efficiency of the ALD thin film found from the absorbance spectra (Figure 2a) related to its compactly arranged WO_3 grains, might also have enhanced the photocurrent.

A more detailed look at the voltammogram under chopped light at 0.8 - 1.2 V vs. RHE is shown in Figure 4c and 4d. Once the light is switched on, the photocurrent rapidly increases for both ALD and sputtered films. For ALD film, the current follows a plateau-like behaviour (Figure 4c), while for the sputtered

film, distinct spikes are seen (Figure 4d). The spikes imply that fast recombination of the photo-generated carriers occurs[55]. To confirm this, photoluminescence (PL) measurements were carried out to investigate the recombination of photo-generated charge carriers. Figure S5 shows the PL spectra of the ALD film, the sputtered film, and the blank FTO. The emission peaks at 415 nm can be attributed to the recombination of the photo-generated electron-hole pairs in the WO_3 film[56]. This is in accordance with the bandgap value 3.0 eV obtained by the Tauc plots (Figure 2b). The PL intensity of the ALD WO_3 film is lower than that of the sputtered film, indicating a lower recombination rate of photo-generated electron-hole pairs.

To further understand this process, Intensity Modulated Photocurrent Spectroscopy (IMPS) was carried out to study the charge transport properties. Figure 4e shows a complex plane plot of the IMPS spectrum for both ALD and sputtered WO_3 thin films. The response appears in two quadrants of the complex plane. Accordingly, the frequency at the apex of the semicircle is related to the time constant of the charge transfer process[23]. The average time photogenerated electrons need to reach the back contact, the electron transit time, τ_D, can be estimated from the following equation[57]:

$$\tau_D = (2\pi f_{min})^{-1} \quad (3)$$

where f_{min} is the frequency at which the minimum in the IMPS plot occurs. The f_{min} of the ALD and sputtered WO_3 are 10 kHz and 5 kHz, respectively. τ_D of the ALD and sputtered WO_3 films are τ_D (ALD) = 1.6×10^{-2} ms and τ_D (sputtering) = 3.2×10^{-2} ms, respectively. These τ_D values are lower than that those reported in the literatures, which are around 1 - 20 ms[23,58], which were measured with similar methods and same light sources. The main reason for this difference might be related to the single and much thinner WO_3 layer of 50 nm in this work compared to the literature (1 - 2 µm). The electron transit in the ALD WO_3 film is about two times faster than that in the sputtered film. Fast electron transfer can improve charge-collection efficiency and thus increase photocurrent density which corresponds to the better performance obtained from the ALD WO_3 film. Moreover, a smaller semicircle in the low frequency region (first quadrant) obtained from ALD film, as shown in the inset of Figure 4e, indicates a lower recombination rate of the photogenerated electrons and holes during the PEC water splitting; this corresponds to the analysis of the voltammograms (Figure 4c and d).

To evaluate the stability of the ALD and sputtered WO_3 film electrodes, photocurrent as function of time (Figure S6) was measured at a single constant potential (1.23 V vs. RHE). The results show that no significant degradation of the current density was found for both ALD and sputtered films during 2 h.

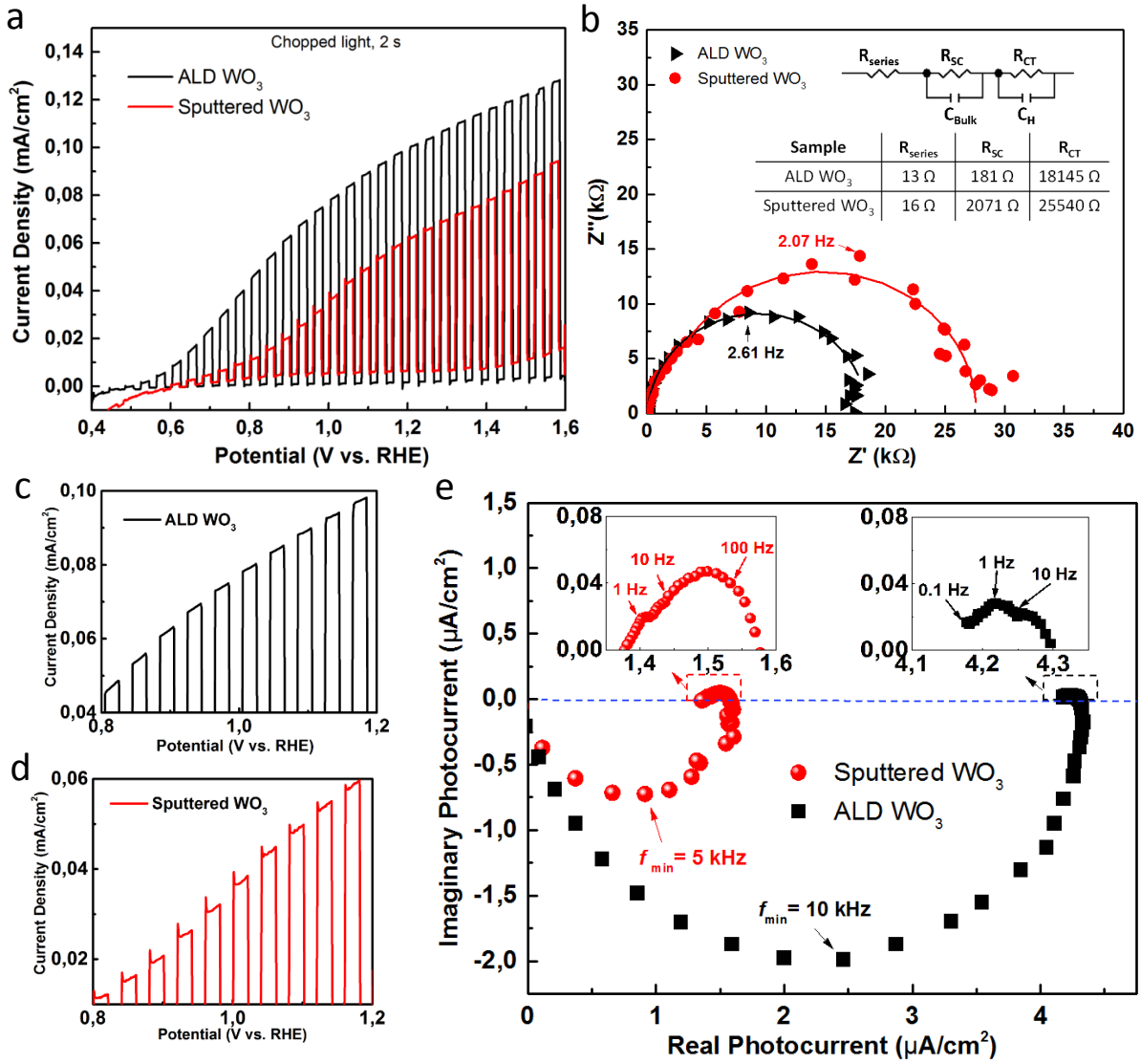

Figure 4. PEC characterization of ALD (black) and sputtered (red) WO_3 thin films: (a) Photocurrent density vs. applied potential curves under chopped light illumination (2 s light on and off, respectively). (b) Nyquist plots of the measured (dots) and fitted (line) impedance spectra at an applied potential of 1 V vs. RHE in the frequency range of 10^{-1} to 3×10^{5} Hz; insets are the equivalent circuit model and the fitting values of R_{series}, R_{SC} and R_{CT}; (c) and (d) are enlargements of the light-on part of the curves in (a) at 0.8 V to 1.2 V vs. RHE; (e) IMPS data at an applied potential of 1.23 V vs. RHE in the frequency range of 10^{-1} to 10^{5} Hz (insets: enlargement of the plot in the first quadrant).

In summary, a higher performance was found for the ALD deposited films compared to the sputtered film. The main reason for the better performance of the ALD film is attributed to less physical defects inside the film and at the interface between the film and the FTO layer. Therefore, electrons transfer is not hindered and electron-hole recombination rate is low.

3.3. Chemical defects

Chemical states and chemical defects, such as the oxidation state and oxygen vacancies, play a sensitive role in the properties of WO_3[12,59,60]. The strong impact of oxygen vacancies on the electrochemical activity of WO_3 was recently also demonstrated in recent DFT studies[37]. In the following study, we annealed the as-deposited WO_3 thin films in different atmospheres, namely N_2, O_2, and air (synthetic air, N_2 mixed with O_2 in the ratio of 4:1), to evaluate the impact of the chemical defects on the PEC performance.

It was found that the grains in ALD films were more homogeneous and compactly arranged than those in the sputtered WO_3 after annealing in the three different atmospheres (Figure S7) corresponding to the comparison in Figure 1. There are no significant differences in the surface morphology among the films annealed in the three different atmospheres. Likewise, the UV-vis spectrophotometry measurements show almost overlapping light absorbance spectra, as shown in Figure S8. The results indicate similar light harvesting properties of the WO_3 films annealed in air, N_2 and O_2, respectively.

The GIXRD analyses (Figure S9) reveal that all the films annealed in different atmospheres show the monoclinic WO_3 diffraction peaks (JCPDS No. 83-0950). No phase separation or impurity phases were observed in the annealed samples, implying little influence on the crystal structures of the three different annealing atmospheres.

To gain more insight into the chemical defects in the WO_3 films inherited by the different annealing atmospheres, the chemical states of O and W were investigated by XPS (Figure S10). The relative content of each component was characterized by the fitted peak areas of the XPS pattern. It can be seen that the content of lattice O (O_L, centered at 530.5 eV) increases and the content of absorbed O (O_A, centered at 532.0 eV) decreases with the annealing atmosphere in the order: N_2, air and O_2, as shown in Figure 5a and 5b. This indicates that the concentration of hydroxyl and oxygen vacancies in the films decreased with the increasing O_2 partial pressure of the annealing atmosphere. In addition, the amount of W^{6+} (centered at 37.8 and 35.7 eV) increases and the amount of W^{5+} (centered at 36.8 and 34.7 eV) decreases with the annealing atmosphere in the order: N_2, air, and O_2 (Figure 5c and 5d) corresponding to the increasing content of O_L for maintaining the charge balance. These XPS results suggest that the concentration of oxygen vacancies decreased in the WO_3 film with increasing O_2 partial pressure of annealing atmosphere.

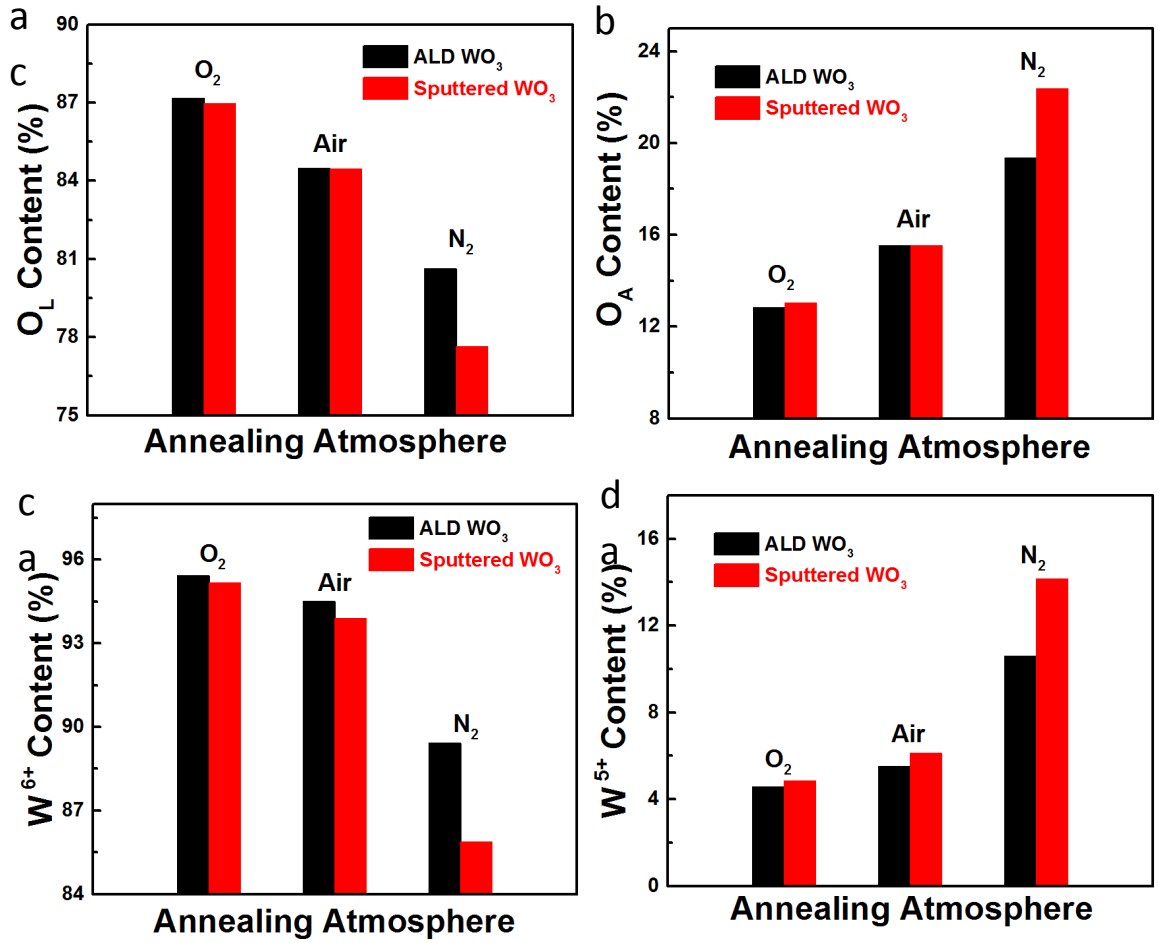

Figure 5. Content histogram from the fitted XPS results of (a) lattice O (O_L), (b) absorbed O (O_A), (c) W^{6+}, and (d) W^{5+} of WO_3 films after annealing in differenct atmospheres: O_2, air, N_2.

The PEC results of the WO_3 thin films annealed in different atmospheres are illustrated in Figure 6. Both ALD and sputtered WO_3 thin films annealed in air show the highest photocurrent density of 0.10 mA/cm^2 and 0.06 mA/cm^2 at 1.23 V vs. RHE, respectively, and the films annealed in N_2 show the lowest photocurrent density of 0.08 mA/cm^2 and 0.04 mA/cm^2 at 1.23 V vs. RHE, respectively. The highest PEC conversion efficiency obtained from the WO_3 thin films annealed in air can be due to the synergistic effect of high concentration of hydroxyl (Figure 5) and appropriate amount of oxygen vacancies on the surface of the films. The enhancement from the oxygen vacancies is believed to be due to its role as shallow electron donor for WO_3 in the band gap[61]. The WO_3 films annealed in N_2, with the highest concentration of oxygen vacancies (as shown in XPS results) show, however, the lowest photocurrent densities. This can be explained by the fact that a very high amount of oxygen vacancies act as electron "traps" to inhibits the electron transfer, thus, decreasing the photocurrent generation[36].

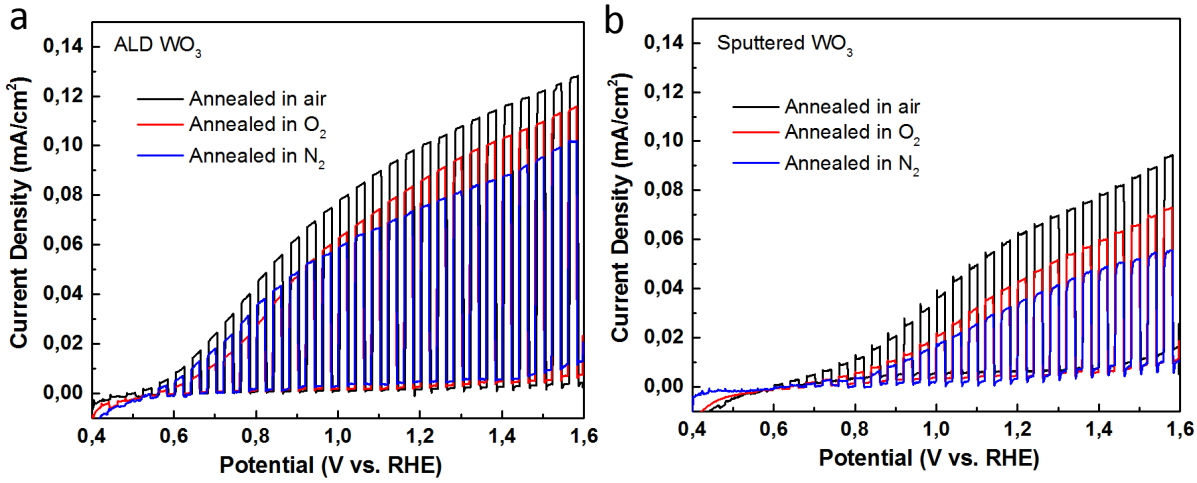

Figure 6. Photocurrent density vs. applied potential of (a) ALD and (b) sputtered WO_3 films annealed in different atmospheres (chopped light measurements with t = 2s).

To confirm this explanation, the charge transfer properties of the ALD films annealed in different atmospheres were evaluated by IMPS. As shown in Figure 7, the f_{min} of the ALD WO_3 films annealed in air, O_2 and N_2 are 10 kHz, 6.3 kHz and 5 kHz, respectively. This corresponds to electron transit times of τ_D = 1.6×10^{-2} ms, 2.5×10^{-2} ms, 3.2×10^{-2} ms, respectively. Hence, the electron transit time is the lowest in the WO_3 film annealed in N_2 and, thus, results in the lowest photocurrent density.

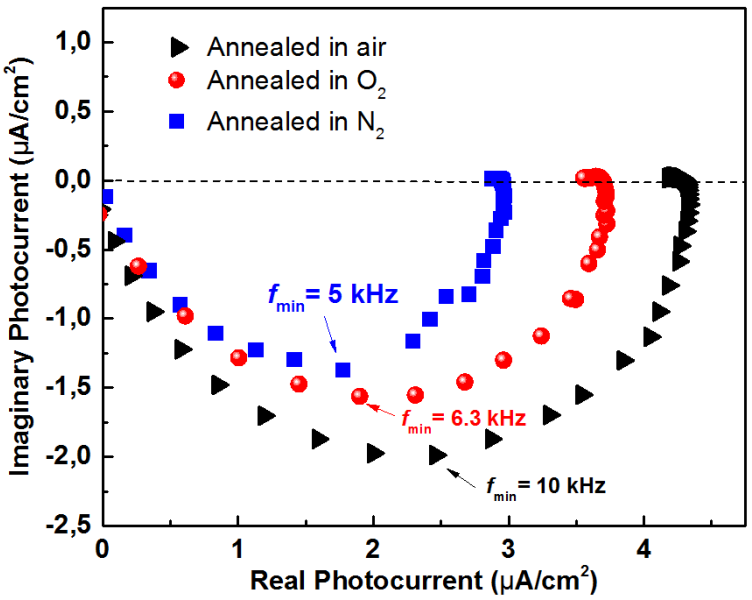

Figure 7. IMPS data of ALD WO_3 films annealed in different atmospheres (applied potential: 1.23 V vs. RHE; frequency range: 10^{-1} to 10^5 Hz).

A comparison of the PEC performance between films annealed in ambient air and in synthetic air is carried out in order to make sure that the origin of the

gases (gas bottle vs. ambient air) is not dominating the results and interpretations. It is found that the photocurrents are rather similar. A slightly higher photocurrent density was measured for the films annealed in ambient air compared to the films annealed in synthetic air (both for ALD and sputtered films) (Figure S11). This can be related to the content of CO_2 and H_2O in the ambient air which could form C-O or H-O groups on the surface during annealing. These groups can enhance the surface activity during the PEC conversion[5].

4. Conclusion

The impact of physical and chemical defects in WO_3 thin film on PEC water splitting properties were studied.

The physical defects were evaluated by comparing the properties of ALD and sputtered thin films. Physical defects, like micro-holes and cracks formed during the deposition process, increased the electron transit time and also resulted in a higher recombination rate at the physical defects which inhibited the photocurrent generation. Hence, for PEC electrode fabrication, it is important to reduce the physical defects in the thin film and make perfect connection between the functional layer and the electron collection layer.

The chemical defects were evaluated by different annealing atmospheres (air, N_2 and O_2). Chemical defects, like oxygen vacancies, can generate more adsorbed OH on the surface of the film and also serve as shallow electron donor to enhance the PEC efficiency. On the other hand, excess amount of chemical defects can act as recombination centres which inhibit the electron transfer, thus, decreasing the photocurrent generation. The oxygen vacancy concentration in the WO_3 films changed according to the annealing atmosphere: N_2 > Air > O_2. The best performance was obtained from films annealed in air indicated an appropriate content of chemical defects. According to these results, it is worth to relate the annealing conditions to the content of chemical defects.

We can conclude that the selection of the thin film deposition process as well as the processing conditions, such as the annealing atmosphere, have significant impact on the performance of the thin films towards water splitting activity. Electrodes should be designed and processed in order to minimize physical defects inside the functional films and at the interface between functional layer and electron conduction layer. This demands for deposition techniques to deposit high quality, defect free thin films and interfaces. In addition, chemical defects should be well tailored, since they can impact the performance in different ways. The obtained results should be transferred from

plain thin films to nanostructured thin films in order to fabricate photoelectrodes with significant higher performance in the future.

ASSOCIATED CONTENT

Supporting Information Available: **SEM images, AFM images, STEM images, Photoluminescence (PL) spectra, Photocurrent density-time curves, UV-vis light absorbance spectra, GIXRD patterns, XPS spectra, Comparison of PEC properties in ambient air and in synthetic air**

Acknowledgement

Y. Zhao and A. Bieberle-Hütter acknowledge the financial support from NWO (FOM program nr. 147 "CO_2 neutral fuels") and from the China Scholarship Council (CSC). The authors thank Nanolab at TU/e for access to SEM and XPS. We thank H. Genuit (DIFFER) for depositing thin films by sputtering, E. Zoethout (DIFFER) for the XPS measurements and results analysis, R.H. Godiksen for the PL measurements, B. Barcones (TU/e) and R.G.R. Weemaes (Philips) for performing the FIB cross-sectioning. Solliance and the Dutch province of Noord Brabant are acknowledged for funding the TEM facility.

References

(1) Lewis, N. S. Research Opportunities to Advance Solar Energy Utilization. *Sci.* **2016**, *351*, 353.

(2) Khaselev, O.; Turner, J. A. A Monolithic Photovoltaic-Photoelectrochemical Device for Hydrogen Production via Water Splitting. *Sci.* **1998**, *280*, 425–428.

(3) Walter, M. G.; Warren, E. L.; Mckone, J. R.; Boettcher, S. W.; Mi, Q.; Santori, E. A.; Lewis, N. S. Solar Water Splitting Cells. **2010**, 6446–6473.

(4) Fujishima, A.; Honda, K. Electrochemical Photolysis of Water at a Semiconductor Electrode. *Nature* **1972**, *238*, 37–38.

(5) Chen, H. M.; Chen, C. K.; Liu, R.-S.; Zhang, L.; Zhang, J.; Wilkinson, D. P. Nano-Architecture and Material Designs for Water Splitting Photoelectrodes. *Chem. Soc. Rev.* **2012**, *41*, 5654.

(6) Li, Z.; Luo, W.; Zhang, M.; Feng, J.; Zou, Z. Photoelectrochemical Cells for Solar Hydrogen Production: Current State of Promising Photoelectrodes, Methods to Improve Their Properties, and Outlook. *Energy Environ. Sci.* **2013**, *6*, 347–370.

(7) Ran, J.; Zhang, J.; Yu, J.; Qiao, S. Z. Enhanced Visible-Light Photocatalytic H_2 production by $Zn_xCd_{1-x}S$ Modified with Earth-Abundant Nickel-Based Cocatalysts. *ChemSusChem* **2014**, *7*, 3426–3434.

(8) Gao, X.; Wu, H. Bin; Zheng, L.; Zhong, Y.; Hu, Y.; Lou, X. W. Formation of Mesoporous Heterostructured $BiVO_4/Bi_2S_3$ Hollow Discoids with Enhanced Photoactivity. *Angew. Chemie - Int. Ed.* **2014**, *53*, 5917–5921.

(9) Xing, Z.; Zong, X.; Zhu, Y.; Chen, Z. G.; Bai, Y.; Wang, L. A Nanohybrid of CdTe@CdS Nanocrystals and Titania Nanosheets with P-N Nanojunctions for Improved Visible Light-Driven Hydrogen Production. *Catal. Today* **2016**, *264*, 229–235.

(10) Mi, Q.; Zhanaidarova, A.; Brunschwig, B. S.; Gray, H. B.; Lewis, N. S. A Quantitative Assessment of the Competition between Water and Anion Oxidation at WO_3 Photoanodes in Acidic Aqueous Electrolytes. *Energy Environ. Sci.* **2012**, *5*, 5694–5700.

(11) Zhu, T.; Chong, M. N.; Chan, E. S. Nanostructured Tungsten Trioxide Thin Films Synthesized for Photoelectrocatalytic Water Oxidation: A Review. *ChemSusChem* **2014**, *7*, 2974–2997.

(12) Wang, G.; Ling, Y.; Wang, H.; Yang, X.; Wang, C.; Zhang, J. Z.; Li, Y. Hydrogen-Treated WO_3 Nanoflakes Show Enhanced Photostability. *Energy Environ. Sci.* **2012**, *5*, 6180.

(13) Bignozzi, C. A. *Photocatalysis*; **2011**; Vol. 7.

(14) Liu, R.; Lin, Y.; Chou, L.-Y.; Sheehan, S. W.; He, W.; Zhang, F.; Hou, H. J. M.; Wang, D. Water

Splitting by Tungsten Oxide Prepared by Atomic Layer Deposition and Decorated with an Oxygen-Evolving Catalyst. *Angew. Chemie Int. Ed.* **2011**, *50*, 499–502.

(15) Wang, S.; Chen, H.; Gao, G.; Butburee, T.; Lyu, M.; Thaweesak, S.; Yun, J. H.; Du, A.; Liu, G.; Wang, L. Synergistic Crystal Facet Engineering and Structural Control of WO_3 Films Exhibiting Unprecedented Photoelectrochemical Performance. *Nano Energy* **2016**, *24*, 94–102.

(16) Zeng, Q.; Li, J.; Bai, J.; Li, X.; Xia, L.; Zhou, B. Preparation of Vertically Aligned WO_3 Nanoplate Array Films Based on Peroxotungstate Reduction Reaction and Their Excellent Photoelectrocatalytic Performance. *Appl. Catal. B Environ.* **2017**, *202*, 388–396.

(17) Hu, D.; Diao, P.; Xu, D.; Wu, Q. Gold/WO_3 Nanocomposite Photoanodes for Plasmonic Solar Water Splitting. *Nano Res.* **2016**, *9*, 1735–1751.

(18) Bignozzi, C. A.; Caramori, S.; Cristino, V.; Argazzi, R.; Meda, L.; Tacca, A. Nanostructured Photoelectrodes Based on WO_3 : Applications to Photooxidation of Aqueous Electrolytes. *Chem. Soc. Rev.* **2013**, *42*, 2228–2246.

(19) Horprathum, M.; Srichaiyaperk, T.; Samransuksamer, B.; Wisitsoraat, A.; Eiamchai, P.; Limwichean, S.; Chananonnawathorn, C.; Aiempanakit, K.; Nuntawong, N.; Patthanasettakul, V.; Oros, C.; Porntheeraphat,S.; Songsiriritthigul, P.; Nakajima, H.; Tuantranont, A.; Chindaudom, P. Ultrasensitive Hydrogen Sensor Based on Pt-Decorated WO_3 Nanorods Prepared by Glancing-Angle Dc Magnetron Sputtering. *ACS Appl. Mater. Interfaces* **2014**, *6*, 22051–22060.

(20) Zheng, J. Y.; Pawar, A. U.; Kim, C. W.; Kim, Y. J.; Kang, Y. S. Highly Enhancing Photoelectrochemical Performance of Facilely-Fabricated Bi-Induced (002)-Oriented WO_3 film with Intermittent Short-Time Negative Polarization. *Appl. Catal. B Environ.* **2018**, *233*, 88–98.

(21) Huang, J.; Zhang, Y.; Ding, Y. Rationally Designed/Constructed CoO_X /WO_3 Anode for Efficient Photoelectrochemical Water Oxidation. *ACS Catal.* **2017**, *7*, 1841–1845.

(22) Zhang, H.; Zhou, W.; Yang, Y.; Cheng, C. 3D WO_3/$BiVO_4$/Cobalt Phosphate Composites Inverse Opal Photoanode for Efficient Photoelectrochemical Water Splitting. *Small* **2017**, *13*, 1–8.

(23) Su, J.; Guo, L.; Bao, N.; Grimes, C. A. Nanostructured WO_3/$BiVO_4$ Heterojunction Films for Efficient Photoelectrochemical Water Splitting. *Nano Lett.* **2011**, *11*, 1928–1933.

(24) Wang, Y.; Tian, W.; Chen, L.; Cao, F.; Guo, J.; Li, L. Three-Dimensional WO_3 Nanoplate/Bi_2S_3 Nanorod Heterojunction as a Highly Efficient Photoanode for Improved Photoelectrochemical Water Splitting. *ACS Appl. Mater. Interfaces* **2017**, *9*, 40235–40243.

(25) Zhang, J.; Ma, H.; Liu, Z. Highly Efficient Photocatalyst Based on All Oxides WO_3/Cu_2O Heterojunction for Photoelectrochemical Water Splitting. *Appl. Catal. B Environ.* **2017**, *201*, 84–91.

(26) Chen, Z.; Ning, M.; Ma, G.; Meng, Q.; Zhang, Y.; Gao, J.; Jin, M.; Chen, Z.; Yuan, M.; Wang, X.; Liu, J.-M.; Zhou, G. Effective Silicon Nanowire arrays/WO_3 Core/shell Photoelectrode for Neutral pH Water Splitting. *Nanotechnology* **2017**, *28*, 275401.

(27) Barreca, D.; Carraro, G.; Gasparotto, A.; Maccato, C.; Altantzis, T.; Sada, C.; Kaunisto, K.; Ruoko, T. P.; Bals, S. Vapor Phase Fabrication of Nanoheterostructures Based on ZnO for Photoelectrochemical Water Splitting. *Adv. Mater. Interfaces* **2017**, *4*, 1–9.

(28) Gui, M. S.; Zhang, W. De; Chang, Y. Q.; Yu, Y. X. One-Step Hydrothermal Preparation Strategy for Nanostructured WO_3/Bi_2WO_6 Heterojunction with High Visible Light Photocatalytic Activity. *Chem. Eng. J.* **2012**, *197*, 283–288.

(29) Valerini, D.; Hernandez, S.; Di Benedetto, F.; Russo, N.; Saracco, G.; Rizzo, A. Sputtered WO_3 Films for Water Splitting Applications. *Mater. Sci. Semicond. Process.* **2016**, *42*, 150–154.

(30) Fabrega, C.; Murcia-Lopez, S.; Monllor-Satoca, D.; Prades, J. D.; Hernandez-Alonso, M. D.; Penelas, G.; Morante, J. R.; Andreu, T. Efficient WO3 Photoanodes Fabricated by Pulsed Laser Deposition for Photoelectrochemical Water Splitting with High Faradaic Efficiency. *Appl. Catal. B Environ.* **2016**, *189*, 133–140.

(31) Carraro, G.; Gasparotto, A.; Maccato, C.; Bontempi, E.; Barreca, D. PECVD of Hematite Nanoblades and Nanocolumns: Synthesis, Characterization, and Growth Model. *Chem. Vap. Depos.* **2015**, *21*, 294–299.

(32) Kwong, W. L.; Qiu, H.; Nakaruk, A.; Koshy, P.; Sorrell, C. C. Photoelectrochemical Properties of WO_3 Thin Films Prepared by Electrodeposition. *Energy Procedia* **2013**, *34*, 617–626.

(33) Sun, M.; Chen, Z.; Bu, Y. Enhanced Photoelectrochemical Cathodic Protection Performance of H_2O_2-Treated In_2O_3 Thin-Film Photoelectrode under Visible Light. *Surf. Coatings Technol.* **2015**, *266*, 79–87.

(34) Hwang, Y. J.; Boukai, A.; Yang, P. High Density N-Si/n-TiO_2 Core/Shell Nanowire Arrays with Enhanced Photoactivity. *Nano Lett.* **2009**, *9*, 410–415.

(35) Coronado, J. M.; Fresno, F.; Hernández-Alonso, M. D.; Portela, R. *Design of Advanced Photocatalytic Materials for Energy and Environmental Applications*; **2013**.

(36) Liu, Y.; Li, J.; Tang, H.; Li, W.; Yang, Y.; Li, Y.; Chen, Q. Enhanced Photoelectrochemical Performance of Plate-like WO_3 Induced by Surface Oxygen Vacancies. *Electrochem. commun.* **2016**, *68*, 81–85.

(37) Kishore, R.; Cao, X.; Zhang, X.; Bieberle-Hütter, A. Electrochemical Water Oxidation on WO_3 surfaces: A Density Functional Theory Study. *Catal. Today* **2018**, No. February, 0–1.

(38) Zhang, X.; Klaver, P.; Van Santen, R.; Van De Sanden, M. C. M.; Bieberle-Hütter, A. Oxygen Evolution at Hematite Surfaces: The Impact of Structure and Oxygen Vacancies on Lowering the Overpotential. *J. Phys. Chem. C* **2016**, *120*, 18201–18208.

(39) Malviya, K. D.; Dotan, H.; Yoon, K. R.; Kim, I.-D.; Rothschild, A. Rigorous Substrate Cleaning Process for Reproducible Thin Film Hematite (α-Fe_2O_3) Photoanodes. *J. Mater. Res.* **2016**, *31*, 1565–1573.

(40) Balasubramanyam, S.; Sharma, A.; Vandalon, V.; Knoops, H. C. M.; Erwin Kessels, W. M. M.; Bol, A. A. Plasma-Enhanced Atomic Layer Deposition of Tungsten Oxide Thin Films Using (^{t}BuN)$_2$ (Me_2N)$_2$W and O_2 Plasma. *J. Vac. Sci. Technol. A Vacuum, Surfaces Film.* **2018**, *36*.

(41) Tuller, H. L. *Photoelectrochemical Hydrogen Production*; van de Krol, R., Grätzel, M., Eds.; Electronic Materials: Science & Technology; Springer US: Boston, MA, **2012**; Vol. 102.

(42) Tauc, J. Optical Properties and Electronic Structure of Amorphous Ge and Si. *Mater. Res. Bull.* **1968**, *3*, 37–46.

(43) Yang, B.; Barnes, P. R. F.; Bertram, W.; Luca, V. Strong Photoresponse of Nanostructured Tungsten Trioxide Films Prepared via a Sol–gel Route. *J. Mater. Chem.* **2007**, *17*, 2722–2729.

(44) Sun, Y.; Murphy, C. J.; Reyes-Gil, K. R.; Reyes-Garcia, E. A.; Thornton, J. M.; Morris, N. A.; Raftery, D. Photoelectrochemical and Structural Characterization of Carbon-Doped WO_3 Films Prepared via Spray Pyrolysis. *Int. J. Hydrogen Energy* **2009**, *34*, 8476–8484.

(45) Somorjai, G. A.; Bratlie, K. M.; Montano, M. O.; Park, J. Y. Dynamics of Surface Catalyzed Reactions; the Roles of Surface Defects, Surface Diffusion, and Hot Electrons. *J. Phys. Chem. B* **2006**, *110*, 20014–20022.

(46) Cui, Y.; Shao, X.; Prada, S.; Giordano, L.; Pacchioni, G.; Freund, H. J.; Nilius, N. Surface Defects and Their Impact on the Electronic Structure of Mo-Doped CaO Films: An STM and DFT Study.

Phys. Chem. Chem. Phys. **2014**, *16*, 12764–12772.

(47) Sun, K.; Saadi, F. H.; Lichterman, M. F.; Hale, W. G.; Wang, H.-P.; Zhou, X.; Plymale, N. T.; Omelchenko, S. T.; He, J.-H.; Papadantonakis, K. M.; Brunschwig, B. S.; Lewis, N.S. Stable Solar-Driven Oxidation of Water by Semiconducting Photoanodes Protected by Transparent Catalytic Nickel Oxide Films. *Proc. Natl. Acad. Sci.* **2015**, 201423034.

(48) Kalanur, S. S.; Hwang, Y. J.; Chae, S. Y.; Joo, O. S. Facile Growth of Aligned WO_3 Nanorods on FTO Substrate for Enhanced Photoanodic Water Oxidation Activity. *J. Mater. Chem. A* **2013**, *1*, 3479–3488.

(49) Stoll, T.; Zafeiropoulos, G.; Dogan, I.; Genuit, H.; Lavrijsen, R.; Koopmans, B.; Tsampas, M. N. Visible-Light-Promoted Gas-Phase Water Splitting Using Porous WO_3/$BiVO_4$ photoanodes. *Electrochem. commun.* **2017**, *82*, 47–51.

(50) Dias, P.; Lopes, T.; Meda, L.; Andrade, L.; Mendes, A. Photoelectrochemical Water Splitting Using WO_3 Photoanodes: The Substrate and Temperature Roles. *Phys. Chem. Chem. Phys.* **2016**, 5232–5243.

(51) Hilaire, S.; Süess, M. J.; Kränzlin, N.; Bieńkowski, K.; Solarska, R.; Augustyński, J.; Niederberger, M. Microwave-Assisted Nonaqueous Synthesis of WO_3 nanoparticles for Crystallographically Oriented Photoanodes for Water Splitting. *J. Mater. Chem. A* **2014**, *2*, 20530–20537.

(52) Zheng, J. Y.; Song, G.; Kim, C. W.; Kang, Y. S. Fabrication of (001)-Oriented Monoclinic WO_3 Films on FTO Substrates. *Nanoscale* **2013**, *5*, 5279–5282.

(53) Zheng, J. Y.; Haider, Z.; Van, T. K.; Pawar, A. U.; Kang, M. J.; Kim, C. W.; Kang, Y. S. Tuning of the Crystal Engineering and Photoelectrochemical Properties of Crystalline Tungsten Oxide for Optoelectronic Device Applications. *CrystEngComm* **2015**, *17*, 6070–6093.

(54) Zheng, J. Y.; Song, G.; Hong, J.; Van, T. K.; Pawar, A. U.; Kim, D. Y.; Kim, C. W.; Haider, Z.; Kang, Y. S. Facile Fabrication of WO_3 Nanoplates Thin Films with Dominant Crystal Facet of (002) for Water Splitting. *Cryst. Growth Des.* **2014**, *14*, 6057–6066.

(55) Peter, L. M. Energetics and Kinetics of Light-Driven Oxygen Evolution at Semiconductor Electrodes: The Example of Hematite. *J. Solid State Electrochem.* **2013**, *17*, 315–326.

(56) Johansson, M. B.; Zietz, B.; Niklasson, G. A.; Österlund, L. Optical Properties of Nanocrystalline WO_3 and WO_{3-X} Thin Films Prepared by DC Magnetron Sputtering. *J. Appl. Phys.* **2014**, *115*.

(57) Krüger, J.; Plass, R.; Grätzel, M.; Cameron, P. J.; Peter, L. M. Charge Transport and Back Reaction in Solid-State Dye-Sensitized Solar Cells: A Study Using Intensity-Modulated Photovoltage and Photocurrent Spectroscopy. *J. Phys. Chem. B* **2003**, *107*, 7536–7539.

(58) Liu, C.; Yang, Y.; Li, W.; Li, J.; Li, Y.; Chen, Q. In Situ Synthesis of Bi_2S_3 Sensitized WO_3 Nanoplate Arrays with Less Interfacial Defects and Enhanced Photoelectrochemical Performance. *Sci. Rep.* **2016**, *6*, 23451.

(59) Zhao, Y.; Feng, Z. C.; Liang, Y.; Sheng, H. W.; Zhao, Y.; Feng, Z. C.; Liang, Y. Laser-Induced Coloration of WO_3. **1997**, *2227*, 1–4.

(60) Tamboli, D.; Seal, S.; Desai, V.; Maury, a. Studies on Passivation Behavior of Tungsten in Application to Chemical Mechanical Polishing. *J. Vac. Sci. Technol. A Vacuum, Surfaces, Film.* **1999**, *17*, 1168.

(61) Deb, S. K. Electron Spin Resonance of Defects in Single Crystal and Thin Films of Tungsten Trioxide. Phys. Rev. B. **1977**, *16* (3), 1020–1024.

Graphical Abstract

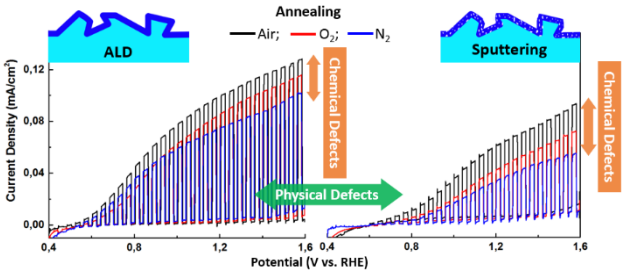

For Table of Contents Only